Title

Exceptional Cycling Performance Enabled by Local Structural Rearrangements in Disordered Rocksalt Cathodes

Journal

Advanced Energy Materials, 12(27)

ISSN

1614-6832

Authors

Ahn, Juhyeon
Ha, Yang
Satish, Rohit
et al.

Publication Date

2022-07-01

DOI

10.1002/aenm.202200426

Exceptional Cycling Performance Enabled by Local Structural Rearrangements in Disordered Rocksalt Cathodes

Juhyeon Ahn,[a] Yang Ha,[b] Rohit Satish,[a] Raynald Giovine,[c] Linze Li,[d] Jue Liu,[e] Chongmin Wang,[d] Raphaele J. Clement,[c] Robert Kostecki,[a] Wanli Yang[b] and Guoying Chen [a,]*

[a] *Energy Storage and Distributed Resources Division, Lawrence Berkeley National Laboratory, Berkeley, California 94720, USA*

[b] *Advanced Light Source, Lawrence Berkeley National Laboratory, Berkeley, California 94720, USA*

[c] *Materials Department, University of California, Santa Barbara, CA 93106, USA*

[d] *Environmental Molecular Sciences Laboratory, Pacific Northwest National Laboratory, Richland, WA 99354, USA*

[e] *Neutron Scattering Division, Oak Ridge National Laboratory, Oak Ridge, TN 37831, United States*

[*] *Corresponding author's email: gchen@lbl.gov*

Abstract

The capacity of lithium transition-metal (TM) oxide cathodes is directly linked to the magnitude and accessibility of the redox reservoir associated with TM cations and/or oxygen anions, which traditionally decreases with cycling as a result of chemical, structural or mechanical fatigue. Here we show that capacity increase over 125% can be achieved upon cycling of high-energy Mn- and F-rich cation-disordered rocksalt (DRX) oxyfluoride cathodes. Our study reveals that in $Li_{1.2}Mn_{0.7}Nb_{0.1}O_{1.8}F_{0.2}$, repeated Li extraction/reinsertion utilizing Mn^{3+}/Mn^{4+} redox along with some degree of O-redox participation leads to local structural rearrangements and formation of domains with off-stoichiometry spinel-like features. The effective integration of these local "structure-domains" within the cubic disordered rocksalt framework promotes better Li diffusion and improves material utilization, consequently increased capacity upon cycling. Our study provides important new insights into materials design strategies to further exploit the rich compositional and structural space of Mn chemistry for developing sustainable, high-energy cathode materials.

1. Introduction

The combined utilization of cationic transition-metal (TM) and anionic oxygen (O) redox processes in Li-excess TM oxides presents new opportunities for the development of high-energy cathode materials for Li-ion batteries (LIBs).[1-3] Li-rich Mn-based $Li_{1+x}(Mn,M')_{1-x}O_2$ ($x > 0$), either forming a layered structure (LMR, M' = Ni, Co, Al etc.) or a cation-disordered rocksalt structure (DRX, M' = d^0 TM such as Nb, Ti, Zr etc.), are particularly attractive due to the natural abundance, low cost and thermal stability of Mn.[4] However, both families of cathodes face significant challenges in maintaining their structural integrity and rate capability upon cycling, with rapid capacity fade, significant voltage hysteresis and impedance rise often accompanying the gradual transformation in local and/or long-range structure upon Li (de)intercalation.[5-8] At the material level, side reactions with the electrolyte, TM reduction and dissolution, TM migration and structural transformation as well as irreversible O redox chemistry, have all been suggested to contribute to these issues.[9-15]

To minimize capacity loss in DRX, increasing Mn redox contribution at the expense of O-based redox processes is an effective strategy, as the former chemistry is inherently more reversible than the latter.[15-18] Fluorine substitution into the O anion sublattice not only stabilizes O redox, as shown by a number of recent studies,[10,18-22] but also lowers the overall anionic valence and allows for an increased amount of Mn to be incorporated into the material. In contrast to the layered structure, F substitution into the cubic DRX structure can easily be achieved during synthesis. Substitution levels up to 10 at.% and 33 at.% have previously been reported on fluorinated Mn-based DRX samples prepared by solid-state and high-energy ball milling synthesis methods, respectively.[10,18,19,20] Although electrochemical performance improvements have been observed even at low levels of F substitution, these oxyfluoride cathodes still suffer from gradual capacity decay during long-term cycling. Upon further increasing F and Mn contents, the charge/discharge voltage profiles evolve quickly with cycling, as shown by recent studies carried out on the $Li_{1.2}$-Mn^{3+}-Nb(Ti)-O-F system.[18,20,23] With up to about 5 at.% F substitution, both voltage and capacity decrease are observed and their trends are similar to that of non-fluorinated DRX.[10,12,19,20] On the other hand, when F substitution level reaches 10 at.%, DRX compound $Li_{1.2}Mn_{0.7}Nb_{0.1}O_{1.8}F_{0.2}$ (denoted as F10 hereafter) delivers a high capacity of more than 250 mAh/g after extended cycling,[20] representing a rare example of LIB cathodes with a capacity retention greater than 100%. The observation opens up new avenues for the development of Mn-based high-energy cathodes, yet such unique cycling behavior remains to be elucidated.

Here, we use a variety of X-ray and electron spectroscopy/microscopy techniques as well as bulk and local structure probes to investigate the evolution of the redox chemistries as well as the chemical and structural origins of unique electrochemical behavior of a Mn-rich $Li_{1.2}Mn_{0.7}Nb_{0.1}O_{1.8}F_{0.2}$ cathode. We reveal that local structural rearrangement and the formation of local "structure-domains" in the three-dimensional cubic DRX framework are responsible for the evolution of the voltage profiles as well as the increase in capacity during cycling. We further discuss the importance of Mn- and F-rich chemistry in enabling favorable Li transport properties and the unique cycling performance in DRX cathodes.

2. Results and discussion

2.1. F10 synthesis and properties

F10 with 10% F substitution in the oxygen sublattice was synthesized by a solid-state method.[20] The cubic rocksalt crystal structure with a $Fm\bar{3}m$ space group was confirmed by powder

X-ray diffraction (XRD) analysis (Fig. 1a). Based on the Rietveld refinement of the XRD pattern, the lattice parameter was determined to be 4.1770 Å, consistent with the previous report.[20]

The local structure of the as-synthesized material was characterized by using solid-state magic angle spinning (MAS) nuclear magnetic resonance (NMR). The ^{7}Li NMR spectrum (Fig. 1b, black line) exhibits a broad signal spanning a frequency range from 2000 to –1500 ppm which is composed of multiple broad and overlapping signals, corresponding to Li nuclei in a variety of local environments in the bulk DRX structure. The distribution of Li environments, highlighted in the pj-MATPASS[24,25] spectrum (grey shading in Fig. 1b), reveals a wide range of ^{7}Li isotropic chemical shift upon suppression of the spinning sidebands. A low amount of diamagnetic Li (about 7% ± 5% of the total integrated ^{7}Li signal intensity) is observed close to 0 ppm (marked with an asterisk), along with the observation of multiple spinning sidebands on both side of the center band, indicating possible presence of Li_2CO_3, LiOH, Li_2O and/or LiF.[26] The amount of diamagnetic Li in F10 is similar to that in the non-fluorinated DRX counterpart ($Li_{1.2}Mn_{0.6}Nb_{0.2}O_2$, F0, approximately 7% ± 5%, Supplementary Fig. 1a), suggesting that the main Li-containing diamagnetic impurity in F10 is unlikely to be LiF. Further insights into the nature of the diamagnetic impurities and the level of F incorporation into the DRX lattice were obtained from ^{19}F solid-state NMR measurements. A broad resonance spanning a wide range of chemical shifts between 1000 and –1000 ppm is observed on the spectrum (Fig. 1c), which can be ascribed to F ions in the bulk DRX structure with a range of local environments. In addition, a sharp signal at an isotropic shift of –204 ppm (marked with an asterisk) with multiple spinning sidebands is also observed, suggesting the presence of a small fraction of LiF-like environments (about 11% ± 5% of the total integrated ^{19}F signal intensity). We note that this is an overestimated value, as our previous work on related DRX compounds[18,19,27,28] showed that NMR signals of F nuclei directly bonded to a paramagnetic species (such as Mn) are too broad and too short-lived to be observed. The majority of the diamagnetic Li signal, therefore, arise from F-free impurities, confirming the near full incorporation of F into the bulk DRX lattice. As the ^{7}Li and ^{19}F NMR spectra collected on $Li_{1.2}Mn_{0.725}Nb_{0.075}O_{1.75}F_{0.25}$ (F12.5) show a significant increase in diamagnetic Li and LiF-like signals (Supplementary Fig. 1b,c), the results further confirm that 10% is near the F solubility limit in solid-state synthesized $Li_{1.2}$-Mn-Nb-O-F series.

To prepare composite cathodes, the as-synthesized F10 powder was first mixed with carbon (in a weight ratio of 8:2) *via* high-energy ball milling. The process largely reduces particle size, as observed with scanning electron microscopy (SEM) (Supplementary Fig. 2a,b), and leads to slight peak broadening on the XRD pattern (Supplementary Fig. 2c). However, the crystal structure and lattice parameter remain unchanged (Supplementary Fig. 2d). The particle-level elemental distribution was determined by using energy-dispersive X-ray (EDX) mapping under a scanning transmission electron microscopy (STEM), which shows that all elements are uniformly dispersed at a single particle level (Fig. 1d). The high angle annular dark field (HAADF)-STEM image and corresponding fast Fourier Transform (FFT) pattern collected near the particle surface region along the [001] zone axis confirm the cubic crystal structure (Fig. 1e).[12,23] In a broad view, the intensity distribution in different atomic columns, visualized by the spot brightness in HAADF-STEM images, appears largely random (Fig. 1e, left). This is consistent with the random distribution of cations clearly shown in the magnified areas i and ii (Fig. 1e, top right). The intensity contrast is likely associated with short-range ordering (SRO) as previously reported in DRX systems.[29,30] For F10, SRO presence is also confirmed by the observation of circle-like diffuse scattering in the FFT pattern (Fig. 1e, bottom right).

2.2. Electrochemical performance

In our previous study,[20] we compared the cycling performance of a series of DRX with varying F substitution: F0 (0%), $Li_{1.2}Mn_{0.625}Nb_{0.175}O_{1.95}F_{0.05}$ (F2.5, 2.5%), $Li_{1.2}Mn_{0.65}Nb_{0.15}O_{1.9}F_{0.1}$ (F5, 5%) and F10 (10%). While both F2.5 and F5 experience a continuous capacity decrease with cycling (Supplementary Fig. 3), which is the typical behavior of LIB cathodes, a considerable improvement in discharge capacity is observed on the F10 cathode that has the highest Mn and F contents in the series. Fig. 2a and b show the electrochemical performance of the F10 cathode when cycled at a current density of 10 mA/g between 1.5 and 4.8 V. The 1st cycle voltage profile displays a slopping curve upon both charge and discharge (blue lines in Fig. 2a) and a single redox couple in the differential capacity versus voltage plot (dQ/dV, Fig. 2b), corresponding to a solid-solution dominated process. Contrary to F2.5 and F5 where the involvement of oxygen redox is evident at the high voltage region above ~ 4.2 V[14,20] during the initial cycles (Supplementary Fig. 3a-d), the intensity of the O redox peak is minimal for F10. Only about 0.75 Li per formula unit (f.u.) or 62% of 1.2 mole Li per f.u. is extracted during the 1st charge. On discharge, nearly 0.57 Li per f.u. or 48% of 1.2 mole Li per f.u. is reinserted. This leads to a low 1st cycle coulombic efficiency of 77% and a specific discharge capacity of 207 mAh/g.

Significant changes in the voltage and dQ/dV profiles are observed upon further cycling. As the number of cycles increases, the voltage regions around 3.0, 4.0 and 4.6 V on charge and 4.0, 3.0 and 1.5 V on discharge become flatter, implying changes in the material's chemistry and/or crystal structure that affect the Gibbs free energy and the Li chemical potential.[31] This is in stark contrast with the smooth sloping voltage curve observed during the 1st cycle. As a result, the discharge capacity increases to over 258 mAh/g after 30 cycles, a net gain of ~ 25%. Substantial capacity increase comes from voltage regions above 3.7 V as well as below 2.9 V. The dQ/dV

peaks in the specific voltage regions aforementioned also evolves when cycled over narrower voltage windows of 1.5–4.6 V, 1.8–4.6 V or 1.8–4.8 V (Supplementary Fig. 4a,b). Although the intensity ratio of the *d*Q/*d*V peaks vary, the cycling-induced capacity increase is observed in all cases (Supplementary Fig. 4c,d). Unsurprisingly, the most drastic changes are observed for the largest voltage window of 1.5–4.8 V while the least amount of change is observed for the smaller window of 1.8–4.6 V. Both high-voltage and low-voltage processes appear to influence the evolution of the redox peaks. On the other hand, the average discharge voltage decreases continuously, with the extent of decrease positively correlated to the total capacity (Supplementary Fig. 4c-f). Upon close examine, voltage decay appears to be more closely related to the lower cutoff voltage, with more severe reduction seen when the cell is discharged to 1.5 V as compared to that of 1.8 V (~ 12% *vs*. 6% loss after 50 cycles, Supplementary Fig. 4e,f).

Similar trend was also observed when increasing current density to 20, 30 or 100 mA/g (Supplementary Fig. 5a-c and f-h). The peak discharge capacity (and discharge energy) are reached after about 30 cycles, with values of 258 mAh/g (716 Wh/kg), 229 mAh/g (634 Wh/kg), 208 mAh/g (574 Wh/kg) and 173 mAh/g (481 Wh/kg) obtained at 10, 20, 30, and 100 mA/g, respectively, corresponding to a capacity retention/energy retention of 1.25/1.12, 1.17/1.05, 1.13/1.03 and 1.09/1.00 (Fig. 2c-f). The evolution of the redox features is less defined when the current density is further increased to 200 or 400 mA/g (Supplementary Fig. 5d,e and i,j). In both cases, a capacity/energy increase is not observed (Fig. 2e,f), indicating kinetic limitation in the cycling-induced chemical/structural changes.

To further understand the kinetic behavior, rate capability tests were performed on the cell after 30 cycles. As the current density increases from 10 to 1000 mA/g, the discharge capacity decreases from 251 to 49 mAh/g (Fig. 3a). The intensity of the redox features near 3 V discharge and 4 V charge remain strong up to a current density of 100 mA/g (Fig. 3b), consistent with the cycling performance shown earlier. The contribution to capacity from the specific voltage regions of 2.5–3.5 V (*A*), 3.5–4.6 V (*B*), 4.6–4.8 V (*C*) on charge and 4.8–3.5 V (*D*), 3.5–2.2 V (*E*), 1.8–1.5 V (*F*) on discharge are shown as a function of the current density (Fig. 3c,d). As the current density increases, the charge capacity in the voltage region *A* decreases while that of region *B* increases (Fig. 3c), indicating that the redox process in region *A* is more rate limiting. At a high current density of 100 mA/g, about twice of the capacity are obtained in region *B* than that in *A*. On discharge, majority of the capacity (~ 70%) is obtained from region *E* at all current densities, with the contribution increasing with higher current densities (Fig. 3d). This suggests that compared to the other cathodic processes in the voltage window, the redox process around 3 V has better kinetics.

Area specific impedance (ASI) analysis was performed by using a hybrid pulse power characterization (HPPC) method.[32,33] This allows us to evaluate the cell resistance arising from ohmic drop, Li-ion diffusion through the electrolyte, and solid-state diffusion within the electrode.[34] The measurements were carried out during the 1st and 30th discharge, using a step size of 0.2 V. The examples at the open circuit voltage (OCV) of 4.16 V and 2.92 V are shown in Supplementary Fig. 6a,b, where voltage and current responses are plotted as a function of time. Fig. 3e shows the measured ASI as a function of depth of discharge (DOD) in F10, and the relationship between ASI and OCV is shown in Supplementary Fig. 6c. For F10, the ASI is generally lower during the 30th discharge process compared to that of the 1st, suggesting improvement in kinetics after cycling. Relatively lower impedance values are recorded at the beginning of discharge state around 4 V, which then reaches the minimum during the flatter voltage region around 3 V where the cathodic peak (*E*) in Fig. 3b is located (Fig. 3e, Supplementary Fig.

6a,b). The results further confirm that the process occurring through the 4 V- and 3 V-regions improves Li transport kinetics. For comparison, an overall increase in the ASI is observed upon cycling F2.5 (Supplementary Fig. 6d,e). The impedance values collected during the 30th cycle are higher than those obtained for the 1st cycle in nearly the entire voltage range (or DOD), which is consistent with what is typically observed on LIB cathode materials.[35,36]

2.3. Understanding cycling-induced capacity increase and improvements in kinetics

2.3.1. Evolution of redox chemistry

As TM cations with a d^0 electronic structure (such as Nb in F10) often serve as structural stabilizers and they are redox-inactive in DRX compounds,[29] here we focus our studies on the evolution of Mn and O redox. *Ex situ* hard X-ray absorption spectroscopy (hXAS) and soft X-ray mapping of resonant inelastic X-ray scattering (mRIXS) measurements were performed at the Mn *K*-edge and *L*-edge, respectively. The samples examined include the pristine F10 cathode (P) and cycled cathodes recovered at the end of 1st charge (C1), 1st discharge (D1), 30th charge (C30) and 30th discharge (D30), with an upper voltage cutoff of 4.8 V for charge and a lower voltage cutoff of 1.5 V for discharge, respectively. On X-ray absorption near-edge structure (XANES) spectra collected on the P, D1 and D30 samples, the Mn *K*-edge energy position at the half-height of normalized intensity, commonly used for determining Mn oxidation state,[5,37] is close to that of the Mn_2O_3 standard containing Mn(III) (Fig. 4a). As expected, the *K*-edge position shifts to a higher energy near that of MnO_2 (Mn(IV)) upon charge (C1 and C30). The values of the charged electrodes are within the error range of the Mn(IV) reference.[5] Fig. 4b shows the evolution of the edge energy as a function of cycle number, confirming an overall Mn^{3+}/Mn^{4+} redox process in the bulk. A more detailed analysis of the Mn *K*-edge data shows that majority of Mn oxidation state increase occurs between OCV and 4.2 V on 1st charge (C1”, supplementary Fig. 7a–c). After that, the changes are insignificant up to the upper cutoff voltage of 4.8 V (C1). Similar evolution is observed during the 30th charge, with nearly identical energy positions observed at the end of charge when the cell is cycled up to 4.6 V (C30’) or 4.8 V (C30, Supplementary Fig. 7d–f). On the other hand, Mn reduction occurs mostly from 3.2 to 1.5 V, showing a continuous edge shift towards lower energy in that window (Supplementary Fig. 7g–i).

Mn *L*-edge mRIXS measurements were carried out in both inverse partial fluorescence yield (iPFY) and total fluorescence yield (TEY) mode to probe the Mn chemical distribution near particle subsurface and surface regions, respectively. The typical probing depth is 100–200 nm for iPFY and 10–20 nm for TEY.[38] The experimental (dotted line) and fitted (solid line) mRIXS-iPFY spectra obtained at the Mn L_3-edge on the P, D1 and D30 electrode samples are plotted in Supplementary Fig. 8a-b. The quantification of the Mn valence is shown in Fig. 4c by fitting the data using a linear combination of Mn reference spectra (Supplementary Fig. 8c). As expected, both discharged cathodes (D1 and D30) primarily consist of Mn^{3+} (pale blue bar, Fig.4c). After the 1st discharge, the presence of Mn^{2+} (blue bar, 7.7% and 27.3% for iPFY and TEY, respectively) and Mn^{4+} (green bar, 7.8% and 6.0% for iPFY and TEY, respectively) are also detected in the subsurface and surface regions. After the 30th discharge, the average oxidation state of subsurface Mn remains close to 3+ while that of the surface Mn is significantly lower (~ 2.6+), with a slight increase in Mn^{2+} content in the former (8.5%) and a much large increase in the latter (45%). The relatively higher Mn^{2+} content is consistent with previous reports on surface Mn reduction during cycling of similar compounds.[9,39] A comparison with data collected on 30th charged sample (C30, 2.6% for iPFY and 28.4% for TEY, Supplementary Fig. 8d,e) further suggests that Mn^{2+} formation predominantly occurs during the discharge process. Our study further reveals the presence of Mn^{4+} cations (6.1% for iPFY and 1.5% for TEY) in D30.

It has been shown that oxygen redox processes in DRX consist of both reversible O^{2-}/O^{n-} ($0 < n < 2$) redox and irreversible O loss.[7,40,41] Here we used *operando* differential electrochemical mass spectrometry (DEMS) analysis and mRIXS mapping to probe the O redox chemistry. DEMS is capable of detecting oxidized O species removed from the lattice and released in the form of O_2 gas during cycling. In this case, while a small amount of O_2 evolution (0.3 mmol per mol DRX) with an onset voltage of ~ 4.3 V is observed during the 1st charge, negligible O_2 release is observed after 30 cycles (Supplementary Fig. 9a-c). In the O *K*-edge two-dimensional mRIXS data, the signal at the excitation energy of 531 eV and the emission energy of ~ 524 eV is often used as a fingerprint for oxidized oxygen (O^{n-}) species.[29,42] In some DRX materials, however, the oxidized O signal is indistinguishable from the TM–O hybridized states which also appear at ~ 531 eV.[43,44] Indeed, in our case, the characteristic features are not easily discernable for the P, C1 or C30 electrode samples (Fig. 4d). To this end, a semi-quantitative analysis of the amount of oxidized O at various states of charge was carried out by comparing the RIXS cut at 531 eV (dotted line in Fig. 4d) with the shoulder peak at ~ 524 eV. Using the RIXS cuts obtained for the P and fully discharged (D1) samples (Fig. 4e and f, respectively) as references, a small intensity increase in the oxidized O features is observed at charge voltages of 4.2 and 4.6 V during the 1st cycle (C1" and C1', respectively, Fig. 4f and Supplementary Fig. 10a). These changes become more pronounced at 4.8 V (C1 in Fig. 4f), suggesting that a significant portion of O oxidation takes place near the end of charge. Similar trend is also observed during the 30th charge (C30, Fig. 4g). The changes are much smaller when cycled to a lower upper cutoff of 4.6 V (C30'), suggesting that most of the O oxidation also occurs near the end of the 30th charge, between 4.6 V and 4.8 V. A comparison of the 531 eV RIXS cuts for the C1, C12 and C30 samples (after the 1st, 12th and 30th charge, respectively, Supplementary Fig. 10b) indicates that while the presence of oxidized oxygen species is clear even after 30 cycles, its intensity decreases after the 1st charge. The observed capacity increase with cycling, therefore, is unlikely a result of more O redox contribution in later cycles.

2.3.2. Evolution of the local structure

Changes in Li environments upon cycling were followed by ^{7}Li solid-state NMR (Fig. 5a). To improve NMR spectral resolution, *ex situ* P, D1, and D30 cathode samples were characterized at a low magnetic field (B_0 = 2.35 T) and a fast sample spinning frequency (ν_R = 60 kHz) to reduce NMR line broadening that occurs because of the strong paramagnetic interactions between the ^{7}Li nuclei and nearby Mn species. Again, the broad resonance on the pj-MATPASS isotropic spectra (grey shading) corresponds to a distribution of Li environments within the DRX structure. The average ^{7}Li chemical shift in the spectrum collected on the P sample is ~ 290 ppm (blue line), consistent with octahedral (O_h) Li site occupancy in DRX. This value increases to ~ 420 ppm in D1 and ~ 500 ppm in D30 (red line), along with an increase in chemical shift distribution. In addition, a small intensity increase between 1000 and 1300 ppm (outlined by the green rectangle) was also observed on both D1 and D30. These results suggest that upon cycling, the average Li environment evolves and the degree of disorder in Li nuclei within the DRX framework increases. The values in the 500 ppm range have previously been reported on cubic spinel-type phases where Li occupies tetrahedral (T_d) 8a sites, such as stoichiometric ordered $LiMn_2O_4$ and Li-excess partially-ordered $Li_{1.68}Mn_{1.6}O_{3.7}F_{0.3}$ and $Li_{1.68}Mn_{1.6}O_{3.4}F_{0.6}$ oxyfluorides.[45-47] While it is possible that an increase in disordering along with the inclusion of spinel-like “structure-domains” can lead to a wider chemical shift distribution, this specific chemical shift range is most often observed on partially-ordered spinels with Li/Mn distribution in the 16c and 16d O_h sites.[48] The study suggests that F10 cycling likely involves partial relocation of Li cations and formation of partially-ordered spinel-like cation arrangements.

Further analysis using time-of-flight neutron diffraction (ND) provides additional evidence for site migration. In order to monitor changes in site occupancy, refinements of all ND patterns were performed based on the face-centered-cubic $Fd\bar{3}m$ space group instead of $Fm\bar{3}m$, including the pristine sample. Upon 1st Li extraction, the lattice parameter decreases from 8.327(2) Å (P) to 8.131(2) Å (C1, Fig. 5b and Supplementary Fig. 11a–d). No additional peaks are detected at the end of charge. After the 1st discharge, the lattice expands to 8.269(2) Å (D1), which is well below the pristine value. Most of the lattice contraction occurs during the 1st discharge, with only small changes are observed upon further cycling. A lattice parameter of 8.255(2) Å is obtained on the D30 sample. Overall, the refined structural parameters shown in Supplementary Table 1 agree well with the structural model with partial displacement of Li to T_d 8a sites and partial Li/Mn occupancy in 16c and 16d O_h sites of the spinel crystal structure. Furthermore, neutron pair distribution function (PDF) patterns collected on the D1 and D30 samples show an increase in the negative nuclear scattering intensity with cycling (Supplementary Fig. 11e,f). This can be attributed to an increase in tetrahedral Li-O and/or Mn-O bonding with a bond length of ~ 1.7 Å, along with various O-O pair distribution with a bond length of ~ 2.3-3.1 Å.[42,48,49]

Complementary insights into the structural rearrangements were also obtained from single-particle studies using TEM and selected area electron diffraction (SAED). Here, the local structure changes were monitored by comparing SAED patterns collected on a pristine (P) and discharged F10 particle recovered after 25 cycles (D25, Fig. 5c). Viewed along the [001] direction, the SAED pattern obtained on P corresponds to a typical DRX structure. In addition to bright Bragg diffraction features, the circle-like diffuse scattering (red triangle) attributed to local SRO is also shown (similar to Fig. 1e). After 25 cycles, the SRO features disappear while additional diffraction features (red arrow) appear along with the initial cubic structure. This is clearly illustrated in the intensity profiles of I (for P) and II (for D25) in Fig. 5c. The new diffraction peaks can be assigned to a spinel-like structure where TMs occupy the T_d sites, consistent with the recent reports.[12,23] We note that observation of structural transformation to spinel-like features in electron diffraction studies is not unique to F10. This was previously shown in other Mn-based DRX cathodes such as $Li_{1.2}Mn_{0.4}Ti_{0.4}O_2$, $Li_{1.2}Mn_{0.625}Nb_{0.125}O_{1.95}F_{0.05}$, and $Li_{1.2}Mn_{0.6}Ti_{0.2}O_{1.8}F_{0.2}$.[12,23]

Local Mn environments and metal-ligand interactions in F10 were further probed by Raman spectroscopy.[50,51] *Ex situ* Raman spectra and their fitting using Voigt functions for P, C1, D1, C30 and D30 electrode samples are shown in Fig. 5d. In the P state, the strong Raman band (blue line) centered around 625 cm^{-1} is assigned to an A_{1g} symmetric stretching mode of the $MnO_{6-\alpha}F_\alpha$ ($0 \leq \alpha \leq 6$) framework.[50] Unlike what is observed in the layered structure,[52-54] the broad shoulder peaks near 516 cm^{-1} (corresponding to E_g vibrations, grey shaded) and 445 cm^{-1} (green shaded) arise from the disordered nature of the rocksalt structure. Deconvoluting Raman spectra collected on disordered materials is inherently challenging due to the broad and overlapping peaks resulting from the wide distribution of coordination environments.[55,56] For F10, the experimental evidence for local structural rearrangements gathered by other techniques serves as a basis to identify the heterogeneous structure in the material. Compared to the P state, the A_{1g} peak and its shoulder for the C1 sample largely shifted towards lower wavenumbers of ~ 614 cm^{-1} and ~ 505 cm^{-1}, in accordance with the expected changes in the Mn octahedra upon Mn^{3+}/Mn^{4+} oxidation. Along with this, new vibrational modes at ~ 665 cm^{-1} (orange shaded) are also observed. The peaks in the spectral range from 660 to 665 cm^{-1} are traditionally associated with A_{2u} asymmetric stretching vibration of MnO_6 octahedron in Li-Mn-O spinel-type phases.[50,51,57-60] This is often seen in off-stoichiometry spinel phases in the presence of crystal defects and anion substitutions,[59-61] which differ from the stoichiometric cubic $LiMn_2O_4$-type spinel or the tetragonal $Li_2Mn_2O_4$ structure formed upon further lithiation.[51,62,63] The presence of this new feature at ~ 665 cm^{-1} therefore not only confirms local structural rearrangement to spinel-like environment but also reveals the off-stoichiometry nature of the formed local structure. For the D1 sample, the shoulder peak further shifts towards a lower wavenumber of ~ 485 cm^{-1} and becomes fully resolved from the A_{1g} peak. A significant reduction in 665 cm^{-1} peak intensity suggests that local “structure-domains” are partially reversible during the charge and discharge process. After 30 cycles, the A_{2u} Raman peak becomes stronger on both discharge (D30) and charge (C30), suggesting an overall growth upon cycling. The substantial increase in the width of half maximum peaks in the lower Raman shift range further implies a greater degree of local disorder (Supplementary Table 2). We note that the presence of this new Raman feature at ~ 665 cm^{-1} is significantly reduced in DRX samples with lower Mn and F contents, as shown in the data collected on the F5, F2.5 and F0 cathodes after 30 cycles (Supplementary Fig. 12). The Raman peak at ~ 620 cm^{-1} shown in the cycled F2.5 and F0 is closer to the location of symmetric stretching vibrations seen in cubic $LiMn_2O_4$-type spinel than that of off-stoichiometry spinel phases.[12] The results suggest that the nature and extent of local rearrangements are sensitive to Mn and F contents as well as the redox chemistry in DRX.

2.4. Discussion

The results presented herein offer new and important insights into the distinctive evolution of chemical, structural and electrochemical properties in Mn-rich DRX oxyfluoride cathodes such as F10. We believe that the combination of a high F content in the oxygen anionic sublattice, the random distribution of cations, the vast presence of Mn and its high mobility are responsible for the structural rearrangements during cycling. Refinement of neutron diffraction pattern along with particle-level electron diffraction pattern indicate partial displacement of Li and TM to the tetrahedral sites. Further characterization through NMR and Raman spectroscopy clearly show local structural changes throughout the bulk particles, with the appearances of new chemical shift and Raman shift spectra that are consistent with cubic Li-Mn-O spinel-type phases. A comparison with the data collected on the pristine DRX containing short-range ordering shows different length scale of the new structure, confirming that the structural rearrangement occurs in local domains rather than in cation clusters. Theses prominent changes in the local structure cannot be explained by individual cation migration.

The process of structural rearrangement initiates during the 1st cycle and continues through the subsequent cycles, enabling a broad integration of local "structure-domains" with off-stoichiometry spinel-like-feature into the cation-disordered cubic rocksalt framework in the long range. This leads to the distinct evolution of voltage regions near 4 V and 3 V,[64,65] similar to what was observed on metastable DRX materials such as $Li_4Mn_2O_5$.[66-68] The arrangements not only create excellent percolation pathways of low activation energy Li migration channels[69-71] but also mitigate Jahn-teller distortion and enhance structural stability,[63,72] leading to better material utilization at a given current density, increased accessible capacity and more than 100% of capacity retention with cycling. It is conceivable that over-lithiation of the off-stoichiometry spinel-like domains occurs upon discharging below 3 V, enabling additional capacity not accounted in the pristine material and contributing to additional discharge capacity. Further studies are needed in order to gain insights on the dynamic evolution of the local domains.

Finally, we wish to make a comparison of the disordered rocksalt to spinel-type transformation occurs in Mn-based DRX cycling *vs*. layered to spinel-like transformation occurs in LMR cycling. While the cation redox process primarily involves Mn^{3+}/Mn^{4+} in the former, the latter is mainly based on Ni^{2+}/Ni^{4+} and/or Co^{3+}/Co^{4+} redox along with a small contribution from the Mn^{3+}/Mn^{4+} process.[5] In LMR, the structural transformation has been linked to property changes such as hysteresis and impedance rise, which leads to material performance issues such as voltage fade, capacity decay and worsening kinetics.[5,15,73-76] While the nature of the formed spinel-like structure is likely different in these two scenarios, the observed kinetic improvement and capacity increase as a result of integration of local "structure-domains" in the highly fluorinated Mn-rich DRX is intriguing. Further studies on the chemical and structural nature of the local structure are needed in order to better understand these unique properties.

3. Methods

3.1 Synthesis

Details on the solid-state synthesis of the DRX cathode materials can be found in a previous publication.[20] Stoichiometric amounts of Mn_2O_3 (99.9%, ACS reagent), Nb_2O_5 (99%, ACS reagent) and poly(tetrafluoroethylene) (PTFE, 6–9 μm particle size, Goodfellow) together with Li_2CO_3($\geq$ 99.0%, ACS reagent) in 10 mol% excess were mixed in ethanol using a planetary ball mill (PM100, 200 rpm for 18 h). The resulting mixture was dried at 80 °C in a vacuum oven, followed by calcination at 1000 °C for 12 h under an argon atmosphere. The heating and cooling rates were set to 5 °C/min. The resulting powder was ground with mortar and pestle in an Ar-filled glove box. The as-synthesized power was mixed with acetylene black (HS-100, Denka) in an 8:2 weight ratio and blended together using a planetary ball mill (300 rpm for 12 h).

3.2. Electrochemical measurements

For composite electrode fabrication, 7:2:1 wt% of carbon-blended DRX, acetylene black (Denka), and polyvinylidene difluoride (PVDF, kynar flex 2801) binder dissolved in *N*-methyl-2-pyrrolidone (Sigma-Aldrich) were mixed at 2000 rpm using a Thinky mixer (AR-100, Thinky Inc.). The resulting slurry was cast onto an aluminum current collector in an Ar-filled glove box and then dried at 120 °C in a vacuum oven. The coin-type half cells (CR2032) were assembled with 1 M lithium hexafluorophosphate ($LiPF_6$) in 1:1 v/v of ethylene carbonate (EC):diethyl carbonate (DEC) (PuriEL, Soulbrain) electrolyte and a microporous trilayer polypropylene/polyethylene/ polypropylene (Celgard 2325) separator. Lithium foil (Alfa Aesar) was used as counter and reference electrodes. The electrochemical measurements were carried out using constant current in various voltage windows as well as using various current densities. The rate capability performance was evaluated in 1.5–4.8 V at a varying current density of 10, 20, 40, 100, 200, 400, and 1000 mA/g. All charge and discharge capacities were calculated based on the net active material loading on the electrode. Area specific impedance was measured using hybrid pulse power characterization. Coin-type half-cells were discharged for 10 s at the current density of 400 mA/g and then relaxed to the open-circuit voltage for 40 s during charge and discharge. The cells were charged for 10 s at 300 mA/g after each discharge steps. This procedure was repeated for every 0.2 V of discharging, and each step was followed by 1 h rest period. The impedance was calculated based on $\Delta V/\Delta I$ value at each discharge pulse, where V is voltage difference for 10 s and I is the discharge pulse current. All the electrochemical data were acquired using a VMP3 battery potentiostat (Bio-Logic science) at room temperature.

3.3. Characterization

X-ray and neutron diffraction. The powder X-ray diffraction was analyzed by a Bruker D2 powder X-ray diffractometer (Cu Kα, 40 kV, 30 mA, $\lambda = 1.54$ Å). The refinement of the XRD patterns was obtained using a Fullprof software. Neutron powder diffraction was performed using the Nanoscale Ordered Materials Diffractometer (NOMAD) at the Spallation Neutron Source at Oak Ridge National Laboratory. Powder samples were loaded into a 3 mm thin-walled quartz capillary. Four 30-min scans were collected at 300 K and then summed together to improve the statistics of the data. Signals from the empty quartz capillary measurement was subtracted as background from the sample measurement and data were normalized by the scattering intensity from a 6 mm vanadium rod to correct for detector efficiencies. The refinement was carried out using TOPAS software version 6.

Solid-state NMR. Solid state NMR spectra of pristine and *ex situ* cycled DRX cathode samples were acquired at $B_0 = 7.05$ T (300 MHz for ^{1}H) using a super wide bore Bruker BioSpin spectrometer equipped with an AVANCE-III console and a 2.5 mm HX MAS probe tuned to ^{19}F (282.4 MHz) and ^{7}Li (116.6 MHz) Larmor frequencies. Additionally, ^{7}Li solid-state NMR spectra of the pristine F10, D1 and D30 samples were acquired at $B_0 = 2.35$ T (100 MHz for ^{1}H) using a wide bore Bruker BioSpin spectrometer equipped with a DMX 500 MHz console and a 1.3 mm HX MAS probe tuned to ^{7}Li (38.9 MHz). For each sample, approximately 12 or 5 mg of material was loaded into a 2.5 mm or 1.3 mm zirconia rotor, respectively, and the rotors were closed using

Vespel caps in an Ar-filled glovebox. To avoid air and moisture exposure during data acquisition, the samples were spun at the magic angle (MAS) at a frequency $\upsilon_R = 30$ kHz (2.5 mm) or 60 kHz (1.3 mm) using dry nitrogen. ^{19}F and ^{7}Li NMR chemical shifts were externally referenced against lithium fluoride standard powder (LiF, $\delta_{iso}(^{19}\text{F}) = -204$ ppm and $\delta_{iso}(^{7}\text{Li}) = -1$ ppm). The solid-state NMR data were processed using the Bruker TopSpin 3.6.0 software and the spectra were fitted using DMfit.[77] Please refer to Supplementary Note 1 for additional details on the solid-state NMR data acquisition parameters used in this work.

SEM and TEM. The SEM images were obtained by a Field Emission Scanning Electron Microscopy (JEOL 7500F) at 15 KV. For TEM observation, the particles were dispensed onto TEM lacey carbon grids in an Ar-filled glovebox to avoid the exposure to air. TEM and STEM imaging and EDX mapping were performed on an aberration corrected JEOL JEM-ARM200CF with an operation voltage of 200 kV. The convergence semi-angle was 20.6 mrad, and the signals with semi-angles spanning from 68 to 280 mrad were collected for STEM-HAADF imaging. The EDS data analysis was performed using the pathfinder software where the overlapped peaks were deconvolved by using the stored standard reference spectra and employing a multiple and linear least-squares fitting method.

Hard and soft XAS. XANES spectra were collected using hard XAS at Stanford Synchrotron Radiation Lightsource (SSRL) beam line 2-2. Extracted electrode samples from the coin cell after electrochemical testing were rinsed with dimethyl carbonate (DMC), dried and sandwiched between Kapton tapes and placed at 45° to the incident X-ray beam. The data was processed using a Sam's Interface for XAS Package (SIXPACK) software. Soft XAS analysis was conducted at SSRL beam line 10-1 and 8-2. Spectral measurements were performed on the 31-pole wiggler with a ring current of 350 mA, a 1000 line mm^{-1} grating monochromator with 20 mm entrance and exit slits, and a 1 mm^2 beam spot. XAS profiles were collected under ultrahigh vacuum (10^{-9} Torr). The data was collected using the Pymca software. For reference, MnO (Mn(II)), Mn_2O_3 (Mn(III)), and MnO_2 (Mn(IV)) powder standards were measured concurrently.

The mRIXS measurements were performed at the iRIXS end station, Beamline 8.0.1 at the Advanced Light Source (ALS). Extracted electrode samples cycled in coin cells were rinsed with DMC, dried, and pasted on the Cu tape, after which the Al current collector was removed from the electrode in Ar-filled glove box. The prepared samples were transferred into the main chamber at the iRIXS end station under vacuum. The emission data were collected by the ultrahigh-efficiency modular spectrometer (HR RIXS) with the excitation energy change every 0.2 eV. The resolution of the excitation and emission energy is 0.35 eV and 0.25 eV, respectively. The mRIXS data was processed using the Igor code developed by the W. Yang group. Mn L_3-edge data was obtained by the inverse fluorescence yield (iPFY) as described in previous work.[78] The Mn L_3-edge total electron yield (TEY) data was collected at the same time. Detailed composition of Mn(II), Mn(III) and Mn(IV) was obtained by fitting the Mn L_3-edge with standard spectra of MnO, Mn_2O_3, and MnO_2.[79] A standard 1 sigma fitting error applies in data processing.

Operando DEMS. The electrodes were prepared by pressing powder mixture of carbon-blended DRX, carbon black (super P, Timcal) conductor, and PTFE (1 μm particle size, Sigma-Aldrich) binder on to the stainless-steel mesh. For cycled samples, the cathodes cycled in a coin cell were extracted and rinsed with DMC. For DEMS, hermetically sealed half cells with a DRX cathode and a Li metal anode were assembled in an Ar atmosphere glove box using custom-designed Swagelok-type cells, as described in previous publications.[14] The cells were assembled with 1 M $LiPF_6$ in 1:1 v/v of EC:DEC (Sigma) electrolyte and a dual layered separator consisting of a microporous monolayer polypropylene membrane (cathode side, Celgard 2500) and quartz filter paper (anode side, Whatman QMA). The cathode active material loadings were approximately 5 mg/cm^2. The cells were cycled at a constant current of 20 mA/g on a Bio-Logic VSP-series potentiostat under positive Ar pressure (≈ 1.2 bar) while any gas evolution was monitored *in situ* using the custom-built DEMS apparatus.[80-82] The cell headspace was sampled every 10 min and any accumulated gases were swept with Ar to the mass spectrometer chamber for analysis.

Raman Spectroscopy. Raman spectroscopy of *ex situ* electrode samples were conducted on Renishaw in-Via^{TM} Qontor® confocal Raman microscope equipped with 633 nm (He-Ne source) and 10 mW laser source. The power of the laser was adjusted to 10 μW to avoid any accidental laser damage. The samples were sealed in Ar atmosphere in a Kurt & Lesker QF25 viewport equipped with a fused silica (quartz) window. Each spectrum is an average of spectra collected over five spots on the sample. The experimental Raman profiles were deconvoluted and fitted using a Voight function.

4. Conclusions

In this study, we report the unique behavior of capacity increase upon cycling of high-energy Mn- and F-rich cation-disordered rocksalt (DRX) oxyfluoride cathodes. In F10 cathode, the source of capacity was attributed to dominant Mn^{3+}/Mn^{4+} redox along with additional contribution from O redox, both of which remained relatively unchanged in the bulk. Comprehensive analysis using a suit of diagnostics techniques delivered robust evidence on the formation of local "structure-domains" with off-stoichiometry spinel-like features, while in the long-range, the cubic disordered rocksalt structure remained. This unique arrangement enables fast

Li-ion movement throughout the three-dimensionally connected Li pathways, leading to distinct changes in the voltage profile. The ability to effectively integrate such local structure into the cubic structure was attributed to the cation disordered Mn- and F-rich chemistry. Our findings provide guidelines on further utilizing Mn-redox based systems for developing next-generation high-energy cathode materials.

ASSOCIATED CONTENT

Supporting Information Available: Additional data, figures, tables and notes including XRD refinements, SEM images and EDX elemental mapping, NMR, hard and soft XAS spectra, Neutron refinements, Raman spectroscopy, and electrochemical performance are included.

Acknowledgements

The authors thank Prof. Bryan D. McCloskey and Matthew J. Crafton at UC Berkeley for helping with the DEMS measurements and the related discussions, Drs. Michaelle S. Everett and Jagjit Nanda at Oak Ridge National Laboratory for helping with the Neutron diffraction measurements, and Drs. Dennis Nordlund, Eric Nelson, Matthew Latimer, Ryan Davis, Leah Kelly and Sami Sainio at Stanford Synchrotron Radiation Lightsource for helping with the XAS measurements. We appreciate the helpful discussions with Prof. Gerbrand Ceder at UC Berkeley. Use of the Stanford Synchrotron Radiation Lightsource, SLAC National Accelerator Laboratory, is supported by the U.S. Department of Energy, Office of Science, Office of Basic Energy Sciences under Contract No. DE-AC02-76SF00515. The NMR studies use shared facilities of the UCSB MRSEC (NSF DMR #1720256), a member of the Materials Research Facilities Network (www.mfn.org). The TEM work was conducted at the William R. Wiley Environmental Molecular Sciences Laboratory (EMSL), a national scientific user facility sponsored by DOE's Office of Biological and Environmental Research and located at PNNL. PNNL is operated by Battelle for the Department of Energy under Contract DE-AC05-76RLO1830. The neutron diffraction studies (at NOMAD) used resources at the Spallation Neutron Source, a DOE Office of Science User Facility operated by ORNL. This work was supported by the Assistant Secretary for Energy Efficiency and Renewable Energy, Office of Vehicle Technologies of the U.S. Department of Energy under Contract No. DE-AC02-05CH11231.

References

1. D. Chen, J. Ahn, G. Chen, *ACS Energy Lett.* **6**, 1358 (2021).
2. Clément, R. J.; Lun, Z.; Ceder, G. *Energy Environ. Sci.* **13**, 345 (2020).
3. P. Rozier, J. M. Tarascon, *J. Electrochem. Soc.* **162,** A2490 (2015).
4. M. M. Thackeray, J. R. Roy, E. Lee, A. Gutierrez, M. He, J. S. Park, B. T. Yonemoto, B. R. Long, J. D. Blauwkamp, C. S. Johnson, Y. Shin, W. I. F. David, *Sustain. Energy Fuels* **2**, 1375 (2018).
5. E. Hu, X. Yu, R. Lin, X. Bi, S. Bak, K.-W. Nam, H. L. Xin, C. Jaye, D. a. Fischer, K. Amine, X.-Q. Yang, *Nat. Energy* **3**, 690 (2018).
6. D. A. Kitchaev, Z. Lun, W. D. Richards, H. Ji, R. J. Clement, M.Balasubramanian, D. H. Kwon, K. H. Dai, J. K. Papp, T. Lei, B. D. McCloskey, W. Yang, J. Lee, G. Ceder, *Energy Environ. Sci.* **11**, 2159 (2018).
7. R. A. House, G. J. Reeds, M. A. Perez-Osorio, J.-J. Marie, E. Biovin, A. W. Robertson, A. Nag, M. Garcia-Fernandez, K.-J. Zhou, P. G. Bruce, *Nat. Energy* **5**, 777 (2020).
8. J. Ahn, J. H. Kim, B. W. Cho, K. Y. Chung, S. Kim, J. W. Choi, S. H. Oh, *Nano Lett.* **17**, 7869 (2017).
9. J. Zhang, Q. Zhang, D. Wong, N. Zhang, G. Ren, L. Gu, C. Schulz, L. He, Y. Yu, X. Liu, *Nat. Commun.* **12**, 3071 (2021).
10. Z. Lun, B. Ouyang, Z. Cai, R. J. Clément, D.-H. Kwon, J. Huang, J. K. Papp, M. Balasubramanian, Y. Tian, B. D. McCloskey, H. Ji, H. Kim, D. A. Kitchaev, G. Ceder, *Chem* **6**, 153 (2020).

11. X.-D. Zhang, J.-L. Shi, J.-Y. Liang, Y.-X. Yin, J.-N. Zhang, X.-Q. Yu, .Y.-G. Guo, *Adv. Mater.* **30**, 1801751 (2018).

12. D.-H. Kwon, J. Lee, N. Artrith, H. Kim, L. Wu, Z. Lun, Y. Tian, Y. Zhu, G. Ceder, *Cell Rep. Phys. Sci.* **1**, 100187 (2020).

13. C. Zhan, T. Wu, J. Lu, K. Amine, *Energy Environ. Sci.* **11**, 243 (2018).

14. M. J. Crafton, Y. Yue, T.-Y. Huang, W. Tong, B. D. McCloskey, *Adv. Energy Mater.* **10**, 2001500 (2020).

15. G. Assat, J.-M. Tarascon, *Nat. Energy* **3**, 373 (2018).

16. B. Ouyang, N. Artrith, Z. Lun, Z. Jadidi, D. A. Kitchaev, H. Ji, A. Urban, G. Ceder, *Adv. Energy Mater.* **10**, 1903240 (2020).

17. D. Chen, W. H. Kan, G. Chen, *Adv. Energy Mater.* **9**, 1901255 (2019).

18. Z. Lun, B. Ouyang, D. A. Kitchaev, R. J. Clément, J. K. Papp, M. Balasubramanian, Y. Tian, T. Lei, T. Shi, B. D. McCloskey, J. Lee, G. Ceder, *Adv. Energy Mater.* **9**, 1802959 (2019).

19. J. Lee, D. A. Kitchaev, D.-H. Kwon, C.-W. Lee, J. K. Papp, Y.-S. Liu, Z. Lun, R. J. Clément, T. Shi, B. D. McCloskey, J. Guo, M. Balasubramanian, G. Ceder, *Nature* **556**, 185 (2018).

20. J. Ahn, D. Chen, G. Chen, *Adv. Energy Mater.* **10**, 2001671 (2020).

21. D. Chen, J. Ahn, E. Self, J. Nanda, G. Chen, *J. Mater. Chem. A* **9**, 7826, (2021).

22. K. Zhou, S. Zheng, F. Ren, J. Wu, H. Liu, M. Luo, X. Liu, Y. Xiang, C. Xhang, W. Yang, L. He, Y. Yang, *Energy Storage Mater.* **32**, 234 (2020).

23. L. Li, Z. Lun, D. Chen, Y. Yue, W. Tong, G. Chen, G. Ceder, C. Wang, *Adv. Funct. Mater.* 2101888 (2021).

24. Z. Gan, R. R. Ernst, *J. Magn. Reson* **123**, 140 (1996).

25. I. Hung, L. Zhou, F. Pourpoint, C. P. Grey, Z. Gan, *J. Am. Chem. Soc.* **134**, 1898 (2012).

26. B. M. Meyer, N. Leifer, S. Sakamoto, S. G. Greenbaum, C. P. Grey, *Electrochem. Solid-State Lett.* **8**, A145(2005).

27. H. Ji, D. A. Kitchaev, Z. Lun, H. Kim, E. Foley, Deok-Hwang Kwon, Yaosen Tian, M. Balasubramanian, M. Bianchini, Z. Cai, R. J. Clement, J. C. Kim, G. Ceder, *Chem. Mater.* **31**, 2431 (2019).

28. R. J. Clément, D. Kitchaev, J. Lee, G. Ceder, *Chem. Mater.* **30**, 6945 (2018)

29. Z. Lun, B. Ouyang, D.-H. Kwon, Y. Ha, E. E. Foley, T. Y. Huang, Z. Cai, H. Kim, M. Balasubramanian, Y. Sun, J. Huang, Y. Tian, H. Kim, B. D. McCloskey, W. Yang, R. J. Clement, H. Ji, C. Ceder, *Nat. Mater.* **20**, 214 (2021).

30. H. Ji, A. Urban, D. A. Ktchaev, D.-H. Kwon, N. Artrith, C. Ophus, W. Huang, Z. Cai, T. Shi, J. C. Kim, H. Kim, G. Ceder, *Nat. Comm.* **10**, 592 (2019).

31. A. V. D. Ven, J. Bhattacharya, A. A. Belak, *Acc. Chem. Res.* **46**, 1216, (2013).

32. J. P. Christophersen, Battery Test Manual For Electric Vehicles, Revision 3. United States.

33. K. G. Gallagher, P. A. Nelson, D. W. Dees, *J. Power Sources* **196**, 2289 (2011).

34. R. Raccichini, M. Amores, G. Hinds, *Batteries* **5**, 12 (2019).

35 Q. Liu, D. Lei, Y. Qin, J. Wen, F. Guo, Y. A. Wu, Y. Rong, R. Kou, X. Xiao, F. Aguesse, J. Bareno, W. Lu, Y. Li, *Nat. Energy* **3**, 936 (2018).

36. J. R. Croy, A. Gutierrez, M. He, B. T. Yonemoto, E. Lee, M. M. Thackeray *J. Power Sources* **434**, 226706 (2019).

37. H. Dau, P. Liebisch, M. Haumann, *Anal. Bioanal. Chem.* **376**, 562 (2003).

38. F. Lin, Y. Liu, X. Yu, L. Cheng, A. Singer, O. G. Shpyrko, H. L. Xin, N. Tamura, C. Tian, T.-C. Weng, X.-Q. Yang, Y. S. Meng, D. Nordlund, W. Yang, M. M. Doeff, *Chem. Rev.* **117**, 13123 (2017).

39. N.-S. Choi, J.-G. Han, S.-Y. Ha, I. Park, C.-K. Back, *RCS Adv.* **5**, 2732 (2015).

40. D.-H. Seo, J. Lee, A. Urban, R. Malik, S.Y. Kang, G. Ceder, *Nat. Chem.* **8**, 692 (2016).

41. E. McCalla, A. M. Abakumov, M. Saubanere, D. Foix, E. J. Berg, G. Rousse, M.-L. Doublet, D. Gonbeau, P. Novák, G. Van Tendeloo, R. Dominko, J.-M. Tarascon, *Science* **350**, 1516 (2015).

42. J. Wu, Q. Li, S. Sallis, Z. Zhuo, W. E. Gent, W. C. Chueh, S. Yan, Y.-d. Chuang, W. Yang, *Condens. Matter* **4**, 5 (2019).

43 E. Zhao, Q. Li, F. Meng, J. Liu, J. Wang, L. He, Z. Jiang, Q. Zhang, X. Yu, L. Gu, W. Yang, H. Li, F. Wang, X. Huang, *Angew. Chem.* **131**, 4367 (2019).

44. D. Chen, J. Wu, J. K. Papp, B. D McCloskey, W. Yang, G. Chen, *Small* **2000656** (2020).

45. Y. J. Lee, F. Wang, C. P. Grey, *J. Am. Chem. Soc.* **120**, 12601 (1998).

46. M. C. Tucker, J. A. Reimer, E. J. Cairns, *J. Electrochem. Soc.* **148**, A951 (2001).

47. H. Ji, K. Wu, Z. Cai, J. Liu, D.-H. Kwon, H. Kim, A. Urban, J. K. Papp, E. Foley, Y. Tian, M. Balasubramaniam, H. Kim, R. J. Clement, B. D. McCloskey, W. Yang, G. Ceder, *Nat. Energy* **5**, 213 (2020).

48. B. Song, G. M. Veith, J. Park, M. Yoon, P. S. Whitfield, M. J. Kirkham, J. Liu, A. Huq, *Chem. Mater.* **31**, 124 (2019).

49. M. Bianchini, F. Fauth, E. Suard, J.-B. Leriche, C. Masquelier, L. Croguennec, *Acta Cryst.* **B71**, 688 (2015).

50. C. M. Julien, M. Massot, *J. Phys.: Condens. Matter* **15**, 3151 (2003).

51. C. M. Julien, M. Massot, *Mater. Sci. Eng. B* **97**, 217 (2003).

52. R. E. Ruther, A. F. Callender, H. Zhou, S. K. Martha, Nanda, J. *J. Electrochem. Soc.* **162**, A98 (2015).

53. E. Flores, P. Novak, E. Berg, J. *Front. Energy Res.* **6**, 82 (2018).

54. Q. Wu, V. A. Maroni, D. J. Gosztola, D. J. Miller, D. W. Dees, W. Lu, *J. Electrochem. Soc.* **162**, A1255 (2015).

55. C.M. Julien, M. Massot, C. Poinsignon, *Spectrochimica Acta Part A* **60**, 689 (2004).

56. N. Mozhzhukhina, J. Kullgren, C. Baur, O. Gustafsson, W. R. Brant, M. Fichtnet, D. Brandell, *J. Raman Spectroscopy* **51**, 2095 (2020).

57. B. Slautin, D. Alikin, D. Rosato, D. Pelegov, V. Shur, A. Kholkin, *Betteries* **4**, 21 (2018).

58. P. K. Nayak, J. Grinblat, M. Levi, O. Haik, E. Levi, Y.-K. Sun, N. Munichandraiah, D. Aurback, *J. Meter. Chem. A* **3**, 14598 (2015).

59. C. V. Ramana, M. Massot, C. M. Julien, *Surf. Interface Anal.* **37**, 412 (2005).

60. M. Molenda, R. Dziembaj, E. Podstawka, L.M. Proniewicz, *J. Phy. Chem. Sol.* **66**, 1761 (2005).

61. X.-D. Zhang, J.-L. Shi, J.-Y. Liang, Y.-X. Yin, J.-N. Zhang, X.-Q. Yu, Y.-G. Guo, *Adv. Mater.* **30**, 1801751 (108). 62. R. Baddour-Hadjean, J.-P. Pereira-Ramos, *Chem. Rev.* **110**, 1278 (2010).

63. M. M. Thackeray, *Prog. Solid St. Chem.* **25**, 1, (1997).

64. M. S. Whittingham, *Chem. Rev.* **104**, 4271 (2004).

65. M. M. Thackeray, W. I. F. David, P. G. Bruce, J. B. Goodenough, *Mat. Res. Bull.* **18**, 461 (1983).

66. M. Freire, N. V. Kosova, C. Jordy, D. Chateigner, O. I. Lebedev, A. Maignan, V. Pralong, *Nat. Mat.* **15**, 173 (2016).

67. M. D-L., M. Freire, Y. Joly, C. V. Colin, H. E. Fischer, N. Blanc, N. Boudet, V. Pralong, P. Bordet, *Chem. Mater.* **30**, 3060 (2018).

68. Z. Yao, S. Kim, J. He, V. I. Hegde, C. Wolverton, *Sci. Adv.* **4**, eaao6754 (2018).

69. W. Zhang, D. M. Cupid, P. Gotcu, K. Chang, D. Li, Y. Du, H. J. Seifert, *Chem. Mater.* **30**, 2287 (2018).

70. A. Urban, J. Lee, G. Ceder, G. *Adv. Energy Mater.* **4**, 1400478 (2014).

71. J. Reed, G. Ceder, *Chem. Rev.* **104**, 4513 (2004).

72. C. Zuo, Z. Hu, R. Qi, J. Liu, Z. Li, J. Lu, C. Dong, K. Yang, W. Huang, C. Chen, Z. Song, S. Song, Y. Yu, J. Zheng, F. Pan, *Adv. Energy Mater.* **10**, 2000363 (2020).

73. J. R. Croy, M. Balasubramanian, K. G. Gallagher, A. K. Burrell, *Acc. Chem. Res*, **48**, 2813 (2015).

74. W. E. Gent, K. Lim, Y. Liang, Q. Li, T. Barnes, S.-J. Ahn, K. H. Stone, M. Mclntire, J. Hong, J. H. Song, Y. Li, A. Mehta, S. Ermon, T. Tyliszczak, D. Kilcoyne, D. Vine, J.-H. Park, S.-K. Doo, M. F. Toney, W. Yang, D. Prendergast, W. C. Chueh, *Nat. Comm.* **8**, 2091 (2017).

75 D. Mohanty, A. S. Sefat, J. Li, R. A. Meisner, A. J. Rondinone, E. A. Payzant, D. P. Abraham, D. L. Wood, C. Daniel, *Phys. Chem. Chem. Phys.* **15**, 19496 (2013).

76. J.-L. Shi, D.-D. Xiao, X.-D. Zhang, Y.-X. Yin, Y.-G. Guo, L. Gu, L.-J. Wan, *Nano Res.* **10**, 4201 (2017).

77. D.Massiot, F. Fayon, M. Capron, I. King, S. L. Calve, B. Alonso, J.-O. Durand, B. Bujoli, Z. Gan, G. Hoatson, *Magn. Reson. Chem.* **40**, 70 (2001).

78. K. Dai, J. Wu, Z. Zhuo, Q. Li, S. Sallis, J. Mao, G. Ai, C. Sun, Z. Li, W. E. Gent, W. C. Chueh, Y.D. Chuang, R. Zeng, Z.-X. Shen, F. Pan, S. Yan, L. F.J. Piper, Z. Hussain, G. Liu, W. Yang, *Joule* **3**, 518 (2019).

79. Q. Li, R. Qiao, L. A. Wray, J. Chen, Z. Zhuo, Y. Chen, S. Yan, F. Pan, Z. Hussain, W. Yang, *J. Phys. D: Appl. Phys.* **49**, 413003 (2016).

80. B. D. McCloskey, A. Valery, A. C. Luntz, S. R. Gowda, G. M. Wallraff, J. M. Garcia, T. Mori, L. E. Krupp, J. Phys. *Chem. Lett.* **4**, 2989 (2013).

81. B. D. McCloskey, D. S. Bethune, R. M. Shelby, G. Girishkumar, A. C. Luntz, *J. Phys. Chem. Lett.* **2**, 1161 (2011).

82. B. D. McCloskey, A. Speidel, R. Scheffler, D. C. Miller, V. Viswanathan, J. S. Hummelshøj, J. K. Nørskov, A. C. Luntz, *J. Phys. Chem. Lett.* **3**, 997 (2012).

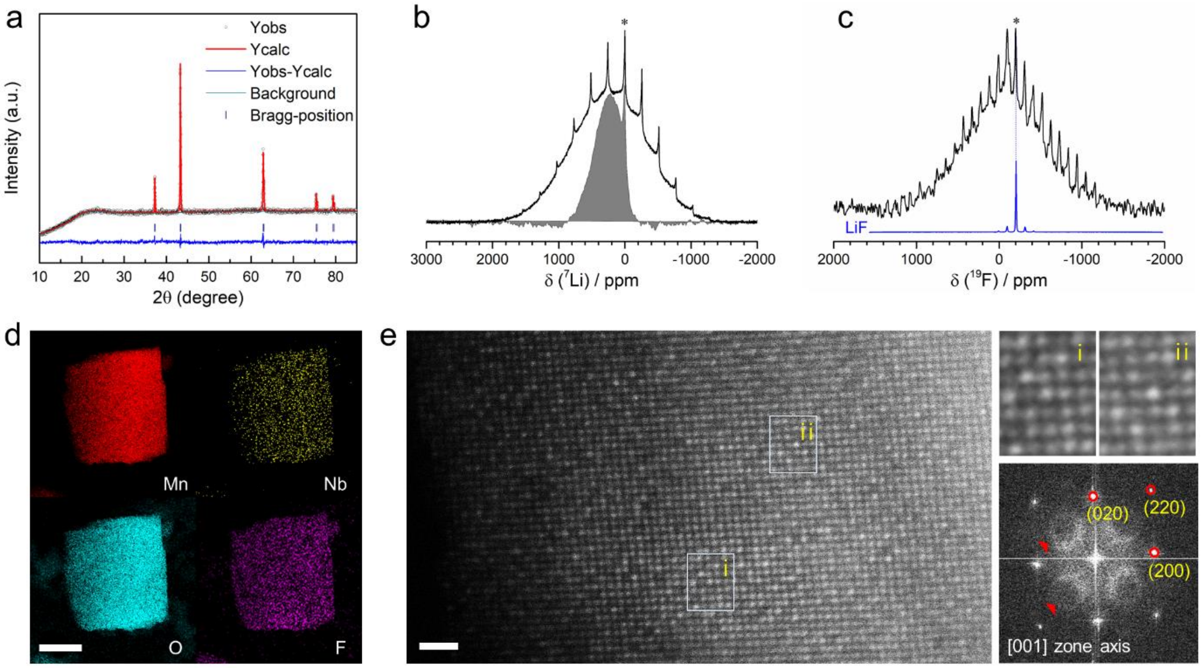

Figure 1. Material characterization. a) Powder XRD refinement of the as-synthesized F10 sample. **b,c**) ^{7}Li and^{19}F MAS NMR spectra collected on as-synthesized F10 powder (black line) at a magnetic field B_0 = 7.05 T with a sample spinning frequency of 30 kHz. Spin echo (^{7}Li) and VOCS (^{19}F) spectra are shown in black. An isotropic ^{7}Li pj-MATPASS spectrum where spinning sidebands are suppressed is shown as a grey shading in (**b**). For comparison, a ^{19}F NMR spectrum collected on standard LiF powder is shown in blue in (**c**). The asterisks indicate a small fraction of diamagnetic impurity signal in both the ^{7}Li and ^{19}F NMR data. **d**) STEM-EDX maps of a single particle for Mn (red), Nb (yellow), O (cyan), and F (magenta) elemental distribution. The scale bar is 200 nm. **e**) HAADF-STEM image and corresponding FFT pattern of a region near the surface of a single particle projected along the [001] zone axis. The scale bar is 1 nm. The magnified images from the areas of i and ii are also shown.

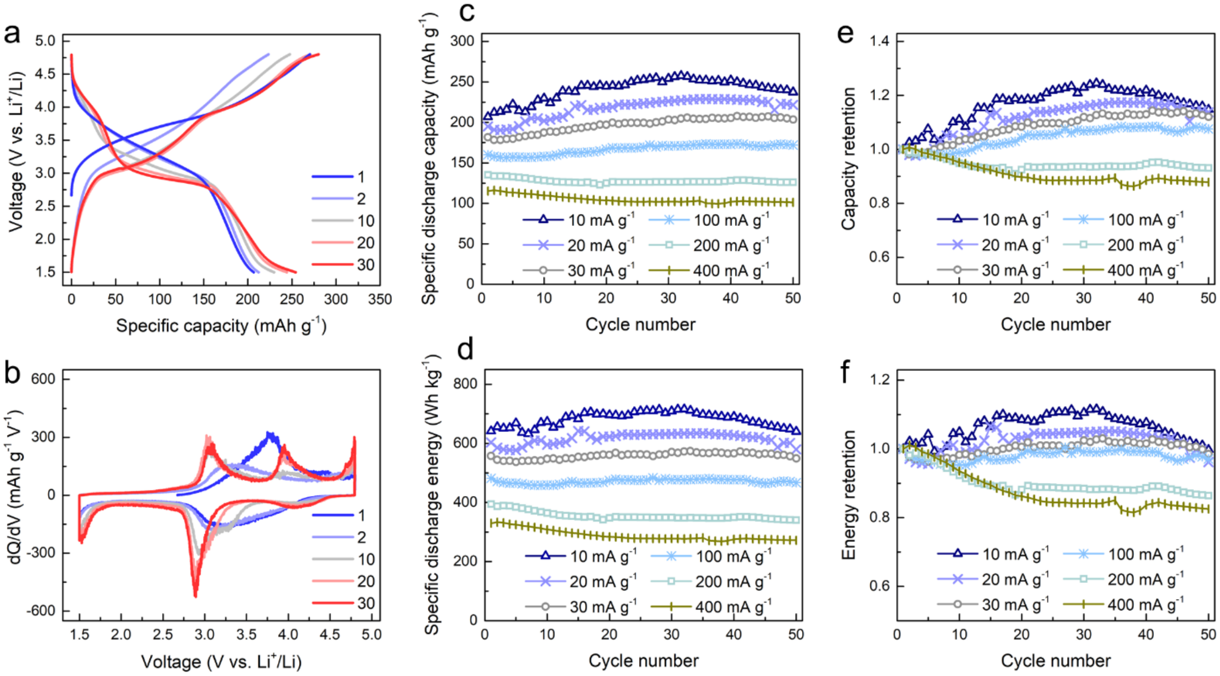

Figure 2. Cycling performance of the F10 cathode. a,b) Voltage profiles and corresponding *d*Q/*d*V plots for the 1st (blue line), 2nd, 10th, 20th and 30th (red line) cycles. The cells were cycled between 1.5 and 4.8 V at a current density of 10 mA g^{-1}. The numbers in the legend indicate the cycle number. **c-f**) Comparison of the (**c**) specific discharge capacity, (**d**) specific discharge energy, (**e**) capacity retention, and (**f**) energy retention during the first 50 cycles between 1.5 and 4.8 V at current densities of 10, 20, 30, 100, 200 and 400 mA g^{-1}.

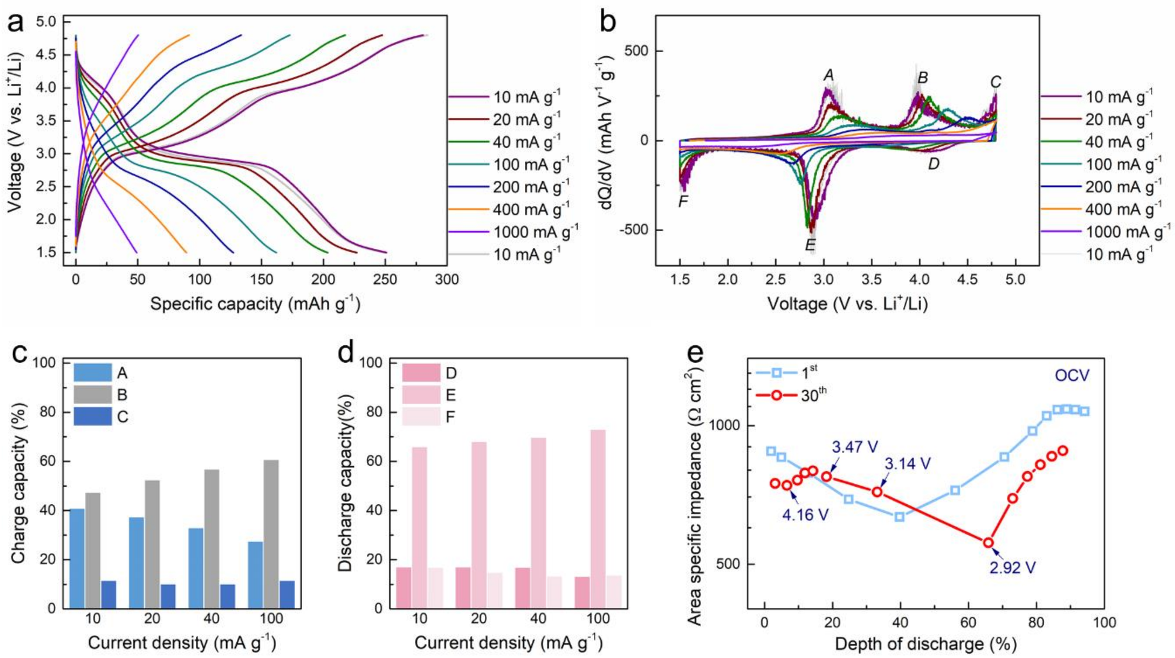

Figure 3. Kinetic properties. a,b) The voltage profiles and corresponding *d*Q/*d*V plots at various current densities collected on the cell after 30 cycles. **c,d**) The charge and discharge capacity portions as a function of current density determined over the following voltage regions: (*A*) 2.5–3.5 V, (*B*) 3.5–4.6 V and (*C*) 4.6–4.8 V on charge, and (*D*) 4.8–3.5 V, (*E*) 3.5–2.2 V and (*F*) 1.8–1.5 V on discharge. **e**) Area specific impedance as a function of the depth of discharge during the 1st (blue) and 30th (red) discharge.

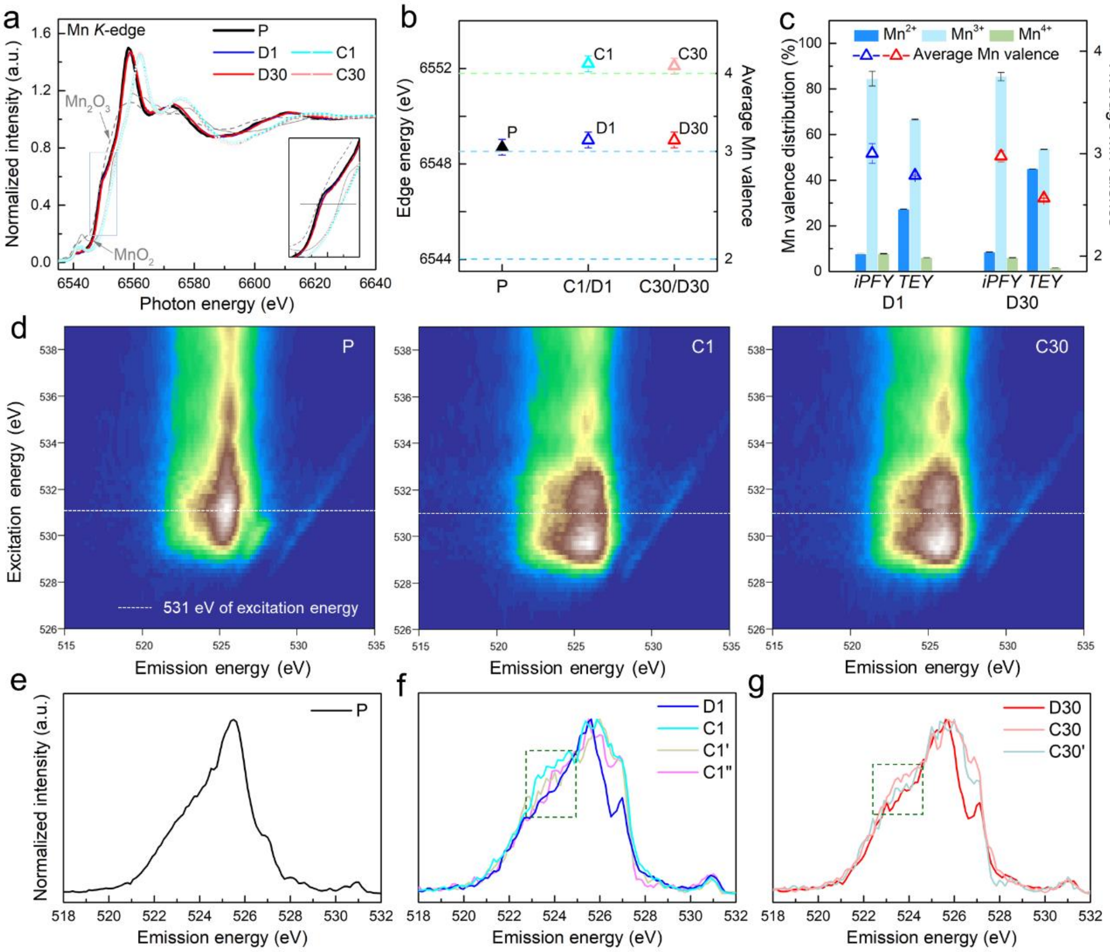

Figure 4. TM and O redox processes. a) Normalized Mn *K*-edge XANES spectra collected on the pristine electrode (P), recovered electrodes after 1st charge to 4.8 V and 1st discharge to 1.5 V (C1, D1), and 30th charged and discharged electrodes with the same cutoff voltages (C30, D30). Reference spectra from Mn^{3+}/Mn^{4+} oxide standards are shown in grey. The enlarged region is shown in the inset. **b**) Mn *K*-edge energy position and average Mn valence as compared to the Mn^{3+}/Mn^{4+} references. **c**) Quantification of the Mn valence distribution and the average Mn valence from Mn L_3-edge mRIXS-iPFY spectra collected on the D1 and D30 electrodes. **d**) O *K*-edge mRIXS data obtained for the P, C1 and C30 electrodes. **e-g**) Normalized O *K*-edge RIXS cuts at an excitation energy of 531 eV for the following samples: (**e**) P, (**f**) C1, D1, and samples obtained on 1st charge to 4.2 V (C1”) and 4.6 V (C1’), (**g**) C30 and D30, and a sample obtained on 30th charge to 4.6 V (C30’). Fingerprint oxidized oxygen features are marked by the dotted area near ~524 eV and TM–O hybridization at 525.5 eV. The C30 and D30 samples were cycled between 1.5 and 4.8 V and C30’ was cycled between 1.5 and 4.6 V at 20 mA g^{-1}, whereas the C1, C1’, C1” and D1 samples were charged or discharged at a current density of 10 mA g^{-1}.

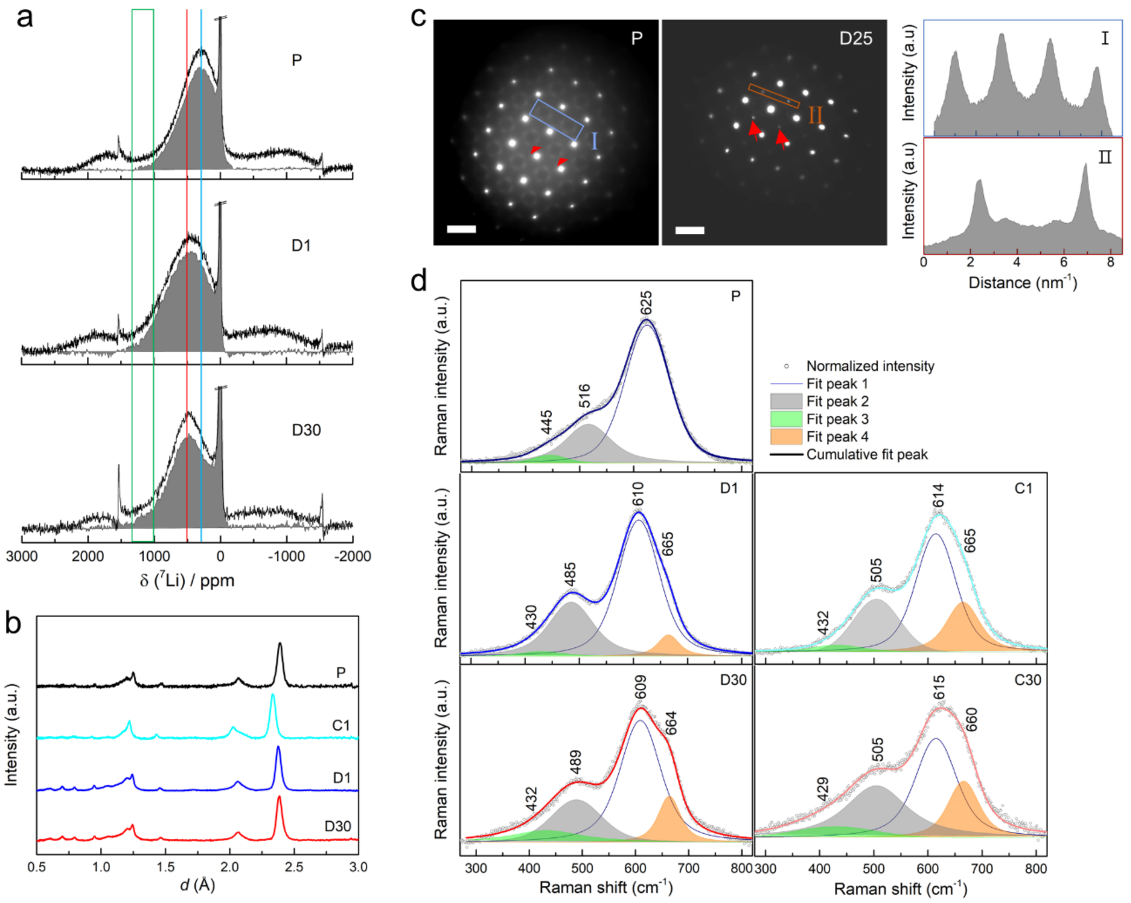

Figure 5. Local structural evolution during cycling. a) ^{7}Li spin echo MAS NMR spectra (black lines) and pj-MATPASS isotropic spectra (grey shaded areas) recorded at a magnetic field B_0 = 2.35 T and a sample spinning frequency of 60 kHz on the pristine (P) cathode, and on samples obtained after the 1st discharge (D1) and 30th discharge (D30) process. The blue, red and green lines at about 290 ppm, 500 ppm, and 1000-1300 ppm, respectively, highlight the evolution of the ^{7}Li resonant frequency with cycling. **b**) Rietveld refinement result of time-of-flight neutron diffraction data collected on electrodes at P, C1, D1 and D30 states. **c**) TEM selected area electron diffraction patterns obtained on the pristine cathode (P) and on an electrode obtained after the 25th discharge process (D25) viewed along [001] zone axis. The scale bar is 5 nm^{-1}. Intensity profiles were obtained from the diffraction regions marked with I and II. **d**) Raman bands for the Mn–O stretching modes collected on the pristine cathode (P) and on electrode samples C1, D1, C30 and D30. Spectra fitting was carried out using Voigt functions.